Evaluation of the use of two-stage calibrated PlanetScope images and environmental variables for the development of the grapevine water status prediction model

Hsiang-En Wei[1], Miles Grafton[1*], Mike Bretherton[1], Matthew Irwin[1] and Eduardo Sandoval[2]

[1] School of Agriculture and Environment, Massey University, Private Bag 11-222, Palmerston North 4442, New Zealand
[2] AgriFood Digital Lab, School of Food and Advanced Technology, Massey University, Private Bag 11-222, Palmerston North 4442, New Zealand
* Corresponding author, E-mail: m.grafton@massey.ac.nz

Abstract

Grapevine water status (GWS) assessment between flowering and veraison plays an important role in viticulture management in terms of producing high-quality grapes. Although satellites and uncrewed aerial vehicles (UAV) have successfully monitored GWS, these platforms are practically limited because data transfer is delayed due to post processing and UAV operation is weather dependent. This study focuses on addressing two issues: the unreliability of GWS estimation using satellite images with low-moderate spatial resolution and the inaccessibility of real-time satellite data. It aims to predict the temporal variation of GWS based on a prediction model using spectral information (calibrated PlanetScope (PS) images), soil/topography data (apparent electrical conductivity, elevation, slope), weather parameters (rainfall and potential evapotranspiration), cultivation practices (irrigation, fertigation, plucking, and trimming), and seasonality (day of the year) as predictors. Stem water potential (Ψstem) was used as a proxy for GWS. Two-stage calibration, including an initial calibration of UAV images with measured Ψstem and a subsequent calibration of satellite images with calibrated UAV data, was applied to calibrate the PS images. Three machine learning models (random forest regression, support vector regression, and multilayer perceptron) were used in the calibration and modeling process. The results showed that a two-stage calibration can generate reliable reference data, with a root mean square error of 113 kPa and 59 kPa on the test sets during the first and second calibration stage, respectively. The prediction model described the temporal variation of block Ψstem when compared with the measured Ψstem. In the similarity analysis, the Pearson correlation coefficient was 0.89 and 0.87 between predicted and reference Ψstem maps across four dates for the two study vineyards. This study supports the concept of developing an approach to predict grapevine Ψstem, which would enable growers to acquire Ψstem variation in advance during the growing season, leading to improved irrigation scheduling and optimal grape quality.

Introduction

Plant water status is widely recognized as an important factor in attaining a high-quality grape due to its role in vegetative growth, partitioning mechanism, berry development, and metabolic composition[1–4]. However, grapevine water status (GWS) exhibits spatial variability across vineyards under a homogeneous irrigation regime, leading to variation in berry development and quality[5,6]. Management of the spatial variability of GWS across vineyards can potentially benefit growers due to berry quality optimization[7,8]. To help achieve optimization of quality, provision of spatial (across vineyards) and temporal (along growing season) GWS monitoring maps would be very useful to the vineyard managers.

Electromagnetic reflectance obtained from remote sensing (RS) platforms, such as satellites and uncrewed aerial vehicles (UAVs), has gained popularity for acting as proxies for GWS. RS techniques enable spatial monitoring of GWS within vineyards, so its application can be applied to develop site-specific irrigation or assist in decision-making for irrigation

management. Compared to satellites, UAVs mounted with sensors have the relative advantages of flexibility in flight scheduling, imagery with a higher spatial resolution (at centimeter-scale), and lower cost of operation. However, UAV surveys are confined to smaller areas due to the short flight endurance imposed by their payload[9]. This may lead to the introduction of non-negligible uncertainty in the radiometric quality of orthoimages resulting from mosaicking a large number of tiles[10]. Satellites, compared to UAVs, are superior when mapping at a larger scale within a single acquisition on a regular basis, guaranteeing radiometric homogeneity for all pixels in the scene[10]. Nevertheless, when considering crops with discontinuous layouts, such as vineyards, satellite imagery with low to moderate resolution cannot be reliably used for plant status description due to the biased assessment originating from the presence of inter-row vegetation and bare soil[11,12]. Although there are some satellites (e.g. GEOSAT-2, GeoEye-1, WorldView-3) that offer images with high resolution and can be used for field monitoring in viticulture, the cost of image acquisition makes it impractical in the application of irrigation scheduling that needs regular monitoring. The

challenge when using RS tools for timely monitoring of highly dynamic phenomena, such as GWS monitoring, is to obtain data that not only has high spatial and temporal resolution but also is affordable and timely accessible.

Pla et al.[13] used UAV data as reference to calibrate Sentinel-2 imagery to quantify damage in rice crops. This study demonstrated that the calibration approach can serve as a viable and cost-efficient alternative to retrieve biophysical variables at large scales. Revill et al.[14] later developed a two-stage method for the calibration of satellite vegetation indices (VIs) to approximate crop leaf area index by calibrating UAV images with ground measurements, followed by calibrating satellite images with calibrated UAV data. This new methodological framework provides an opportunity to integrate the advantages of both satellites and UAVs by utilizing UAV data to help bridge ground truthing and satellite images. This will enable variables of interest to be retrieved at a larger scale, while removing the spectral response of the inter-row elements during the calibration process. This will enhance the reliability of the use of satellite data for plant status monitoring. Based on the study of Revill et al.[14], Bukowiecki et al.[15] transferred this approach to green area index estimation based on the data collected over four growing seasons. The satellite-based prediction model achieved a high performance (coefficient of determination of 0.82). Mazzia et al.[16] used a convolutional neural network to refine satellite-based normalized difference vegetation index maps by utilizing UAV-derived information. They found the refined maps could better describe crop status in terms of correlation analysis and ANOVA, in comparison to the raw satellite images. However, the delivery of satellite imagery to the end user is not in real-time after the fields are sensed. There are often delays in data transfer to the ground station, handling, and distribution to the user, while some processes (such as geometric, radiometric, and atmospheric corrections) are needed before image analysis[17]. In addition, the application of satellite imagery over open fields is weather-dependent and illumination sensitive. Cloud and fog interference is a common restriction imposed on the usability of satellite-based data for crop monitoring. This requires the user to wait for the next revisit of data acquisition[18,19]. These constraints are likely to compromise the practicability of the satellite imagery for growers and viticulturists, despite the satellite images being calibrated with ground truthing. Thus, there is a clear requirement to develop tools for GWS forecasting to promote precision irrigation and thus berry quality.

To potentially address the inaccessibility of satellite-based data caused by unfavorable weather, one way is to develop a GWS prediction model using a soil water balance. As GWS is an integrative response to soil moisture availability, water usage by plants, evaporation, atmospheric transfer, and canopy structures[20], there is a potential to simulate the changes in GWS along a growing season by using these variables as predictors. Precipitation, irrigation, and fertigation replenish soil water content, thus positively impacting GWS[21]. Evapotranspiration (quantifying the net loss of water vapor from evaporation and plant transpiration) accounts for the dynamics and interrelationships of weather components, vegetation expression, and soil properties[22]. Soil properties and topography have persistent effects on the spatial distribution of soil water, which determines the soil moisture

availability to plants, and thus may influence GWS[23]. Cultivation management, such as leaf plucking and trimming, alters canopy vigor, shoot distribution, and total leaf area, leading to the regulation of water consumption level by grapevines[24]. Seasonality, noted as day of the year (DOY), has been found to explain a large part of the variability in GWS[25].

Machine learning (ML) models have recently been extensively used in RS applications due to their ability in modeling both linear and non-linear relationships[26]. These models can be applied to multi-dimensional problems, so they can potentially simulate spectral, spatial, and temporal variabilities between images from different platforms, as well as the complex relationships between GWS and predictors. Previous studies have shown the potential of using UAV or satellite-derived VIs to assess GWS[12,23,27–32]. However, these assessments were mostly limited to identifying the relationships between UAV-based or satellite-based data, and GWS, without considering the need for real-time monitoring which is constrained by the time required for post-processing and associated weather-dependent issues. Most of the RS platforms are currently not able to provide real-time information which is especially important in the context of dynamic GWS monitoring. This study aims to provide GWS prediction based on two-stage calibrated satellite images, which caps off the two previous studies[33,34] with a prediction tool to assist growers and viticulturists in irrigation scheduling or related management decisions for vineyards. Wei et al.[33] focused on identifying the most related spectral features with changes in GWS, and it turned out that they dispersed across multiple spectral bands and needed to be computed collectively using multivariate models. Wei et al.[34] highlighted the importance of ancillary variables (vegetation data, temporal trends, weather parameters, and soil/terrain characteristics) in helping a multispectral sensor describe the variation of GWS. The procedures of this study undertaken were (i) using two-stage calibration (based on ML models) to acquire calibrated satellite images exhibiting GWS estimations for a series of acquisition dates across the first growing season. (ii) developing a GWS prediction model by regressing against the calibrated satellite images acquired in the first growing season using ML models. (iii) evaluating this prediction model by validation with a second set of ground measurements independently collected in the second growing season. To the authors' knowledge, this is the first study that a two-stage calibration approach has been employed to calibrate satellite images for developing GWS prediction models based on ancillary information collected in the first growing season, along with independent evaluation with data collected the second growing season.

Materials and methods

The Context of the Study Vineyards and Study periods

The study vineyards are located at Martinborough in the Greater Wellington Region (lower North Island) in New Zealand (NZ). Both vineyards are sited on a complex of recent alluvial soils overlying gravels, located close to the Ruamahanga and Huangarua Rivers (Fig. 1). The study site contains two commercial vineyards owned by Palliser Estate, named Wharekauhau and Pencarrow. Our study areas in these two vineyards are 6.6 and 6.7 ha, respectively. Pinot Noir was

Page 2 of 14

Wei et al. Technology in Agronomy 2023, 3:6

Fig. 1 Location of study vineyards (Source: Esri, USGS).

chosen as the target variety in this study, due to its requirement for relatively precise GWS management. The Pinot Noir vines in both vineyards were planted in the vineyards in 1998−2000 and two-cane vertical shoot positioned. Inter- and intra-row planting space is 2.2 × 1.6 m for Wharekauhau and 2.2 × 1.8 m for Pencarrow. The annual growth cycle of grapevine in NZ comprises budburst, shoot growth, and flowering (September–November), fruit set and veraison (December–February), followed by berry development and harvesting (March–May). From flowering to veraison, the management of GWS critically determines the final berry quality[35,36]. The study periods span 15th November 2020 to 2nd February 2021 for the first growing season (2020/2021) and 23rd November 2021 to 21st January 2022 for the second growing season (2021/2022). This study focused on cultivation practices, including irrigation, fertigation, plucking, and trimming, due to their potential effects on GWS. Both vineyards are drip-irrigated, with the distance between drippers being 0.6 m. The drip rate is 1.2 L/hr for the drippers in Wharekauhau, and 1.3 L/hr for the drippers in Pencarrow. The irrigation events took place for 2.5 hours on each irrigation date. Fertigation was applied to provide additional nutrients, and lasted for 6 hours on each date of fertigation. Leaf plucking was implemented to remove 80% of the leaves at one side of the canopy to allow sprays better access to grapevines. Trimming was carried out on top of, and on both sides of, canopies to control vegetative growth. Weather information and cultivation practice events are displayed in Fig. 2.

Measured data

Stem water potential (Ψstem) was chosen as an indicator for GWS because it has been reported as a comprehensive expression for early water deficit in vines during the day[37]. Several healthy vines were sampled in grids to assess variability across the vineyards for each measurement date (Table 1) using

two mature and fully expanded leaves from the middle part of each sampled canopy. These leaves are more representative of the canopies. A pressure chamber (model: 610, MPS, Albany, NY, USA) was used between 13:00 and 15:30 to acquire Ψstem (kPa). Prior to the measurement, the sampled leaves were covered with sealable plastic bags for approximately 1 h. The mean value of the two leaf measurements per vine represents the canopy Ψstem. A total of 85 and 63 separate canopies were sampled in the first and the second growing season, respectively. Each of their trunk locations was recorded using a global navigation satellite system (GNSS) with real-time
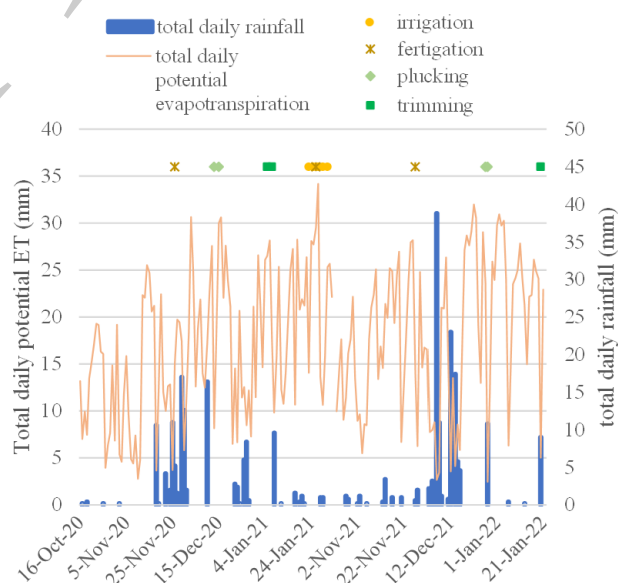
Fig. 2 Total daily potential evapotranspiration and total daily rainfall provided by an on-site weather station, with cultivation practices implemented during the two growing seasons.

Table 1. Details of data acquisition for measured Ψstem, DJI Phantom 4 multispectral UAV imagery, and PlanetScope satellite imagery. The orange outlines indicate the UAV-satellite image pairs used in the second calibration. UAV is uncrewed aerial vehicle.

Acquisition Date	Data Source	Time Gap (day)
15/11/2020	Satellite	–
16/11/2020	Satellite	–
27/11/2020	Measured/ UAV	–
02/12/2020	Satellite	–
04/12/2020	Measured/ UAV	1
05/12/2020	Satellite	
15/12/2020	Satellite	–
17/12/2020	Satellite	–
31/12/2020	Satellite	–
04/01/2021	Satellite	–
14/01/2021	Measured/ UAV/ Satellite	0
15/01/2021	Satellite	–
22/01/2021	Measured/ UAV	1
23/01/2021	Satellite	
26/01/2021	Satellite	–
01/02/2021	Measured/ UAV	1
02/02/2021	Satellite	
23/11/2021	UAV	–
29/11/2021	Measured/ UAV	–
09/12/2021	Measured/ UAV	–
11/01/2022	Measured/ UAV	–
21/01/2022	Measured/ UAV	–

kinematic (RTK) correction (model: GPS1200+, Leica Geosystems AG., Heerbrugg, Switzerland).

UAV-based data

UAV images were collected between 11:00 and 13:00 under cloudless conditions to minimize the impacts of sun angle and shadow. UAV flights and Ψstem measurements were operated on the same dates to ensure comparability (Table 1). The reflectance, with a spatial resolution of 0.05 m, was recorded by a DJI Phantom 4 multispectral UAV (DJI, Shenzhen, China) with six built-in sensors, including blue (450 ± 16 nm), green (560 ± 16 nm), red (650 ± 16 nm), red edge (730 ± 16 nm), and near-infrared (840 ± 26 nm) regions. An integrated sunlight sensor on the top of the UAV records irradiance in the same bands captured by the multispectral sensor during the flight. This information enables UAV images to be normalized and allows

for comparison between images taken under different illumination conditions. Pix4Dmapper (Pix4D SA, Lausanne, Switzerland) was used to apply photogrammetric processing to the UAV data to generate digital surface models (DSM), digital terrain models (DTM), and reflectance maps. To increase imagery spatial accuracy, several ground control points were obtained by GNSS-RTK for each vineyard, and post-imagery alignment was performed in ArcGIS Pro 2.9 (ESRI, Redlands, California, USA).

The vineyards are characterized by discontinuous vegetation surfaces, requiring separation of canopy pixels from grass and soil pixels to obtain pure information of grapevines. As there is a height difference between grapevines and their surrounding components, canopy height can be acquired by subtracting DTM from DSM, then creating binary imagery to exclude background pixels. There are 16 vegetation indices, chosen according to the frequency of usage in viticulture[38], shown in Table 2 and calculated based on pure canopy pixels using "zonal statistic as table" in ArcGIS Pro.

Satellite-based data

PlanetScope (PS) imagery was chosen for this study mainly due to its high spatial and temporal resolution. PS Constellation, owned by Planet, is composed of approximately 200 "Dove" microsatellites, operating in sun-synchronous orbits and able to provide daily land surface imagery at nadir for the entire Earth, passing the equator between 9:30–11:30 (local solar time)[54]. The product used in this study is PS Analytic Ortho Scene Surface Reflectance, which consists of level 3B images recorded by instrument PSB.SD in coastal blue (431–452 nm), blue (465–515 nm), green I (513–549 nm), green II (547–583 nm), yellow (600–620 nm), red (650–680 nm), red edge (697–713 nm), and near-infrared (845–885 nm) bands. These images are acquired with a ground sample distance of 3.7–4.1 m and then resampled to 3.0 m for distribution. This product is orthorectified to remove geometric distortions, and its positional accuracy is less than 10 m RMSE at the 90th percentile. Radiometric corrections are applied to convert pixel values to at-sensor radiance, while atmospheric corrections are implemented to acquire surface reflectance values. Although PS imagery is superior in terms of spatiotemporal resolution, there is radiometric inconsistency due to cross-satellite differences in spectral response, radiometric quality, and orbital

Table 2. List of vegetation indices used in this study.

Vegetation Index	Formula	Reference
Red Edge Chlorophyll Index	(NIR/Red edge) − 1	[39]
Difference Vegetation Index	NIR − Red	[40]
Enhanced Vegetation Index	$2.5 \times (NIR − Red)/(NIR + 6 * Red − 7.5 \times Blue + 1)$	[41]
Excess Green Index	$2 \times Green − Red − Blue$	[42]
Green Normalized Difference Vegetation Index	(NIR − Green)/(NIR + Green)	[43]
Modified Chlorophyll Absorption Ratio Index	$((Red\ edge − Red) − 0.2 \times (Red\ edge − Green)) \times (Red\ edge/Red)$	[44]
Modified Soil Adjusted Vegetation Index	$(2 \times NIR+1 − ((2 \times NIR + 1)^2 − 8 \times (NIR − Red))^{1/2})/2$	[45]
Modified Triangular Vegetation Index	$1.2 \times (1.2 \times (NIR − Green) − 2.5 \times (Red − Green))$	[46]
Normalized Difference Red Edge Index	(NIR − Red edge)/(NIR + Red edge)	[47]
Normalized Difference Vegetation Index	(NIR − Red)/(NIR + Red)	[48]
Normalized Difference Green/Red Index	(Green − Red)/(Green + Red)	[40]
Optimized Soil Adjusted Vegetation Index	(NIR − RED)/(NIR + Red + 0.16)	[49]
Red: Green Ratio	Red/Green	[50]
Simple Ratio	NIR/Red	[51]
Transformed Chlorophyll Absorption Reflectance Index	$3 \times ((Red\ edge − Red) − 0.2 \times (Red\ edge − Green) \times (Red\ edge/Red))$	[52]
Visible Atmospherically Resistant Index	(Green − Red)/(Green + Red − Blue)	[53]

configuration[55,56]. This heterogeneity was addressed in this study by incorporating the radiometric variability in the modeling processes. PS Images, covering the study vineyards and obtained on 13 different days over the study period in 2020/2021, were selected for further analysis after cloud and cloud shadow screening (Table 1).

Soil and Terrain Data

An EM38-MK2 is an electromagnetic induction (EMI)-based sensor (Geonics Ltd., Mississauga, Ontario, Canada). The return reading, apparent soil electrical conductivity (EC_a), is considered a function of soil texture, soil solution, and soil water content[57]. EC_a was used as a proxy to estimate the spatial variation of GWS[58]. In this study, the EM38-MK2 was operated in the vertical dipole mode, with the instrument taking integrated EC_a measurements at about 1.5 m depth. An EMI survey was undertaken by towing the EM38-MK2 at the back of an all-terrain vehicle, with a Trimble Yuma tablet (including an onboard GPS receiver) to geo-reference all EC_a points (mS/m). The vineyards' subsurface infrastructure was confirmed with the vineyard manager to ensure there was no interference from buried metal objects. EC_a points were measured approximately every 3−10 m along transects that were 10 m apart. Point values less than 0 mS/m were removed before interpolation. The geostatistical interpolation method, Empirical Bayesian Kriging, was used to convert point data into a raster with 1 m resolution.

Elevation (m) for the vineyards was obtained from the 'Wellington LiDAR 1m DEM (2013−2014)' layer provided by Land Information New Zealand data service (https://data.linz.govt.nz/). This digital elevation model (in 1 m resolution) was created by aerial LiDAR for the Greater Wellington region (captured between 2013 and 2014). Slope (degree) information was derived based on elevation.

Meteorological and Temporal Data

Weather data was recorded by the on-site weather station (175.4741, −41.2247 WGS84) established by HARVEST.com (http://harvest.com/). The variables captured include rainfall (mm) and potential evapotranspiration (PET; mm). Rainfall was assumed to be homogeneous across the two vineyards. PET, based on the recordings collected by the weather station, was provided by HARVEST.com. PET represents the energy-driven water demand for evapotranspiration by a short green crop[59]. The temporal dependence of GWS on dates through the season was represented by DOY.

Regression Modeling

Random forest regression (RFR), support vector regression (SVR), and multilayer perceptron (MLP) were employed for the image calibration model and Ψstem prediction model in this study. They were implemented using "RandomForestRegressor", "SVR" and "MLPRegressor" from the sklearn library in Python 3.9. As the performance of models is influenced by their hyperparameters, hyperparameter tuning was undertaken beforehand to prevent overfitting. This enabled these ML models to exploit their potential. Grid searching on the training set with 10-fold cross-validation was used to search for the best set of hyperparameters. The test dataset was set aside during hyperparameter tuning and model training. These hyperparameters would then be used on the test set for evaluation of the model's generalization performance. This technique was carried out using "GridSearchCV" from the sklearn library in Python. For each modeling in the two-stage calibration and prediction model, samples were split as training and test sets using a 70/30 ratio. The split was implemented and stratified according to the date of measurement, to ensure that both training and test sets had corresponding percentages of samples for each date. The splitting process was undertaken using "train_test_split" from the sklearn package in Python. All predictor variables were standardized to have mean values equivalent to 0 and a standard deviation of 1 before modeling.

Evaluation

To compare the performance of the image calibration models and the Ψstem prediction models, root mean square error (RMSE) values were computed by applying the trained models with optimized hyperparameters to the test set. The models with the lowest RMSE were chosen for further analysis. To measure the similarity of Ψstem between predicted maps (obtained from the Ψstem prediction model) and the reference maps (acquired in 2021/2022), comparisons were conducted cell by cell using Pearson correlation. The closer the value of the correlation coefficient (r) to ±1, the stronger the linear relationship. This correlation was implemented using "pearsonr" from the scipy library in Python.

Processing Workflow

To develop the Ψstem prediction model, two-stage calibration modeling was carried out (Fig. 3). It was assumed the measured Ψstem data accounts for spatial and temporal variation of Ψstem across the two vineyards over the study periods, and the relationships between Ψstem and spectral data are stable. First, 0.05m resolution UAV images were calibrated using measured Ψstem data collected during 2020/2021 (n = 85) and 2021/2022 (n = 63), respectively (Fig. 3a). The calibrated 0.05m UAV images (Fig. 3b) were used as reference images for the calibration of satellite images and the validation of the Ψstem prediction model. The calibrated 0.05m UAV images acquired during 2020/2021 (n = 4), representing Ψstem estimation, were subsequently downscaled to 3m resolution for spatial matching with the satellite images (Fig. 3c), by spatially averaging the pixel values in the corresponding cells of the PS 3m grids. Next, these downscaled 3m UAV images (n = 4) were used to calibrate the PS images obtained in 2020/2021 (Fig. 3e). All calibrated PS images (n = 13; Fig. 3f) obtained in the study period during 2020/2021 were then used to develop the Ψstem prediction model (Fig. 3). The developed model (Fig. 3) was then validated by the downscaled 3m UAV images (n = 5) acquired during 2021/2022 (Fig. 3i). These were generated by spatially aggregating the calibrated 0.05m UAV images acquired in 2021/2022 (Fig. 3).

Calibration of 0.05m UAV Images

Prior to the first calibration, models were developed by regressing the corresponding 16 VIs, DOY, EC_a, elevation, and slope against measured Ψstem data using RFR, SVR, and MLP (Fig. 3a). For each grapevine trunk position, the mean values of EC_a, elevation, slope, and 16 vegetation indices based on the pure canopy pixels within 0.5 m distance of the trunk were computed for modeling. The acquisition of specific canopy pixels was carried out by overlapping the buffer zones (using recorded trunk location as the center of a circle with a radius of 0.5 m) with the binary raster of canopy height described in section 2.3.
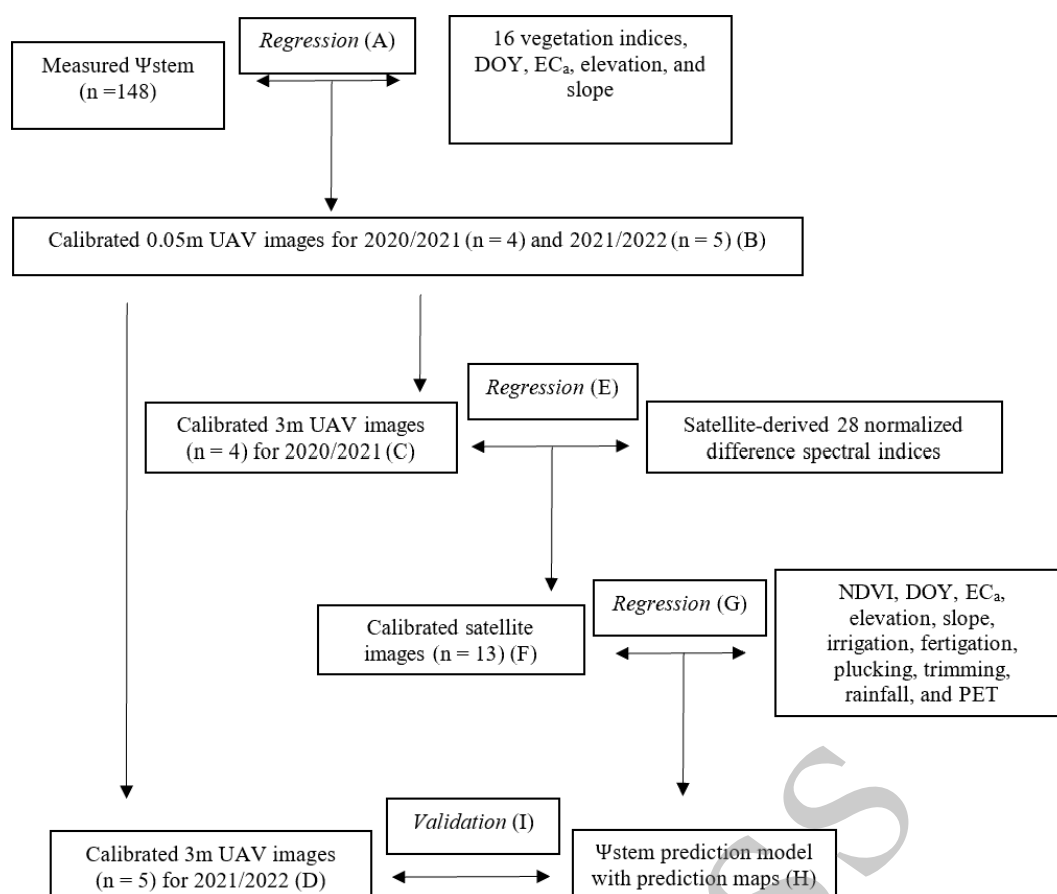
Fig. 3 Overview of the workflow. UAV is uncrewed aerial vehicle; DOY is day of the year; NDVI is normalized difference vegetation index; EC$_a$ is apparent electrical conductivity; PET is potential evapotranspiration.

The models with the best performance (in terms of RMSE on the test sets) were developed separately for the first growing season (2020/2021) and the second growing season (2021/2022). These models were then used to calibrate the UAV images acquired during 2020/2021 (n = 4) and 2021/2022 (n = 5) (Fig. 4a), respectively, to obtain calibrated UAV images exhibiting Ψstem estimation across the vineyards at 0.05m resolution (Figs 3b; 4b).
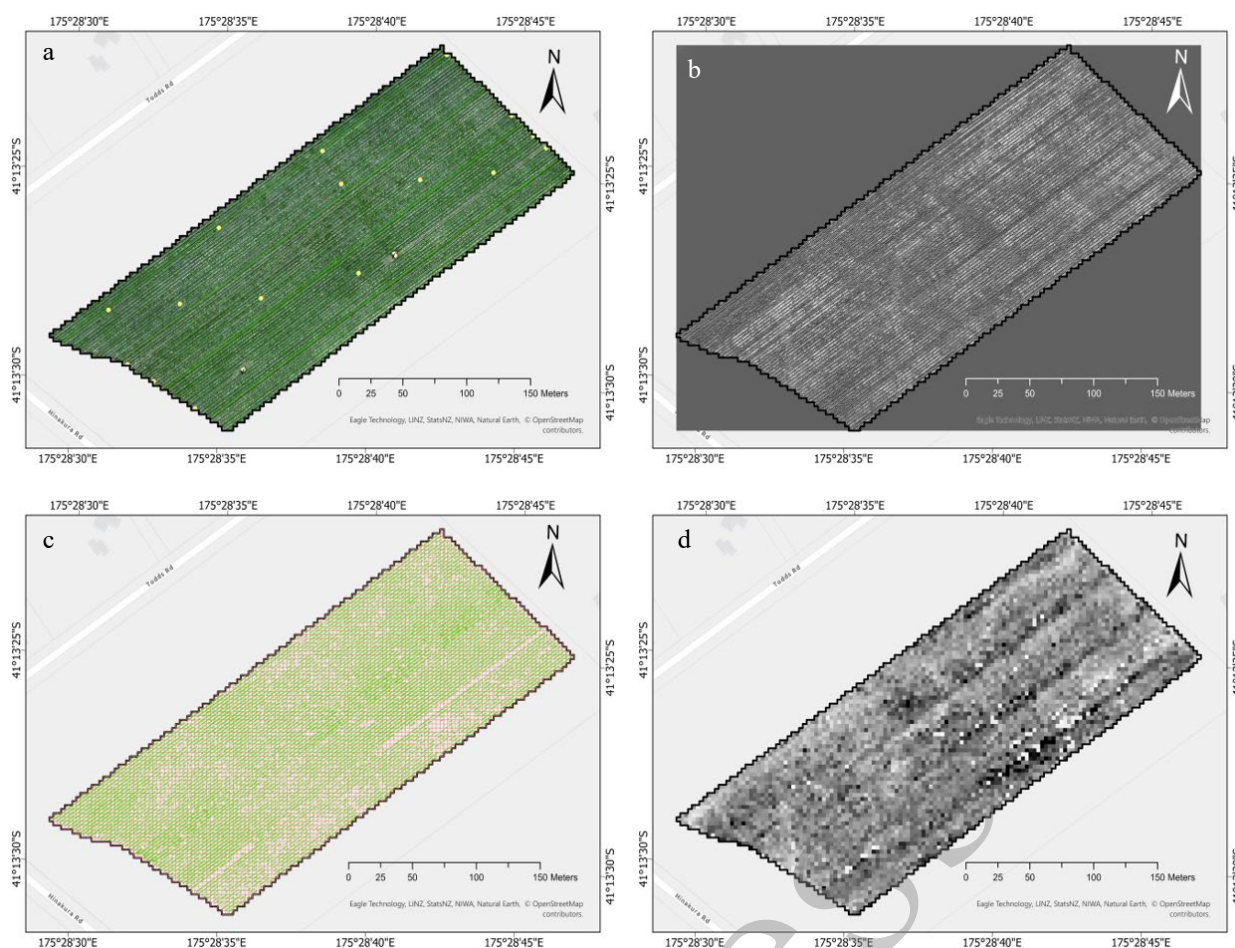
Generation of Downscaled 3m UAV Images

To proceed with the second calibration for UAV-satellite image pairs (Table 1), image co-registration is an essential step. Since UAV images are more spatially accurate due to correction by ground control points, it is a good practice to register the PS images onto the UAV images. In ArcGIS Pro, the UAV images were first resampled from 0.05 m to 3 m resolution and were then used as reference images for the alignment of the PS images. All PS images were then re-aligned with the resampled 3m UAV images using "Snap Raster". Grids of the 3 m pixels were generated by vectorizing the reference images using "Raster to Point" and "Create Thiessen Polygons". As the pixel size of the PS images (3 m) was an integer multiple of that of the UAV images (0.05 m), every PS pixel corresponded to 3,600 UAV pixels after co-registration.

To remove the pixels that did not represent grapevines, the canopy polygons were created based on the binary raster of canopy height obtained in section 2.3 using "Raster to Polygon" for each UAV survey day. These canopy polygons were used to clip the corresponding calibrated UAV images obtained in

section 2.9.1 to acquire canopy pixels representing grapevines (Fig. 4c). Those UAV canopy pixels residing in the same cell of the 3m grids were averaged using "Spatial Join". Nine downscaled 3m UAV images (four images in 2020/2021 and five images in 2021/2022) were created (Fig. 3c & d); Fig. 4d). These downscaled UAV images, representing Ψstem variability across the vineyards at 3 m resolution, served as references for the calibration of PS images in 2020/2021 (Fig. 3e) and for the validation of Ψstem prediction in 2021/2022 (Fig. 3i).

Calibration of satellite images

For the second calibration, models were developed by regressing 28 normalized difference spectral indices (NDSIs) derived from every pixel of the PS images (n = 4; indicated by orange outlines in Table 1) against the reference Ψstem values derived from the 3m calibrated UAV images (n = 4) acquired in 2020/2021 using RFR, SVR, and MLP (Fig. 3e). NDSIs were computed using all possible pairwise-band combinations in the PS images using "combinations" from the itertools package in Python. The UAV-satellite image pairs had at most one day apart in acquisition date to minimize spectral differences (Table 1). The developed models with the best performance (in terms of RMSE on the test sets) were used to calibrate all the PS images (n = 13) acquired during 2020/2021. The series of calibrated satellite images (Fig. 3f), representing Ψstem estimation at 3 m resolution, was subsequently used as the response variable in the development of the Ψstem prediction model.

Fig. 4 An illustration of generating a downscaled 3m UAV image for each UAV survey date. 4a: the UAV image is presented as RGB composites, with measured Ψstem presented as yellow points. 4b: the calibrated 0.05m UAV image exhibiting Ψstem estimation. 4c: the green pixels are pure pixels representing grapevines after clipping pixels of interrow, overlaid with 3m red grids. 4d: the downscaled 3m UAV image after spatial aggregation of pixels in red grids.

Development of Ψstem Prediction Model

Ψstem prediction models were developed by regressing DOY, NDVI, EC_a, elevation, slope, total daily rainfall, total daily PET, irrigation, fertigation, plucking, and trimming events, against the reference Ψstem values derived from the calibrated satellite images (Fig. 3g). NDVI was selected because it is a widely used proxy for vegetation performance which can partially explain the variation in GWS[60]. The underlying assumption of the Ψstem prediction model is that EC_a, elevation, and slope are static during the growing seasons by taking advantage of the temporal stability in the spatial patterns of both NDVI and EC_a[61,62]. NDVI needs to be collected at the beginning of each growing season. During any period in the growing season, managers then rely on weather forecasts for estimating total daily irrigation and PET as well as expected cultivation practices (including irrigation, fertigation, plucking, and trimming) to predict the variation of Ψstem in vineyards.

NDVI, EC_a, elevation, and slope were computed based on the pure canopy pixels within each cell of the 3 m grids. Total daily rainfall, total daily PET, irrigation, fertigation, plucking, and trimming on each day of the 30-day period before the date of Ψstem prediction were used as independent predictors. Plucking and trimming events were noted using one-hot encoding (1 to mark the event and 0 if the event did not occur).

The total number of predictor variables was 125 (Table 3).

Results

Results Variation of Measured Ψstem Values

Both vineyards were visited nine times over two growing seasons, from flowering in late November to veraison in late January. Figure 5 displays the variability in Ψstem collected from 148 canopies at the two vineyards, and the distribution of the measurements on each date. The maximum and minimum observation of Ψstem is 1344 and 310 kPa in 2020/2021, and 1086 and 293 kPa in 2021/2022, respectively. Overall, there is an increasing trend of dehydration in GWS with time for both growing seasons, indicating the increasing presence of water deficit in the grapevines. The only exception is an increase in hydration on 9th December 2021 (compared to the previous measurement) due to rainfall events before sampling (i.e., 38.8 mm on 6th December 2021 and 11 mm on 7th December 2021). In Fig. 5, the height of the box (the difference between the upper quartile and lower quartile) represents the spatial variation of Ψstem on one date across the relevant vineyard. This difference increased as the survey proceeded, implying spatial variation within the vineyards became more pronounced as water deficit increased. The mean values of

Table 3. A summary for the predictors used in developing the Ψstem prediction model. DOY is day of the year; NDVI is normalized difference vegetation index; ECa is apparent electrical conductivity; PET is potential evapotranspiration.

Predictor	Note	Number
DOY	The number is added on along the growing season.	1
NDVI	Collected in late November for the 2020/2021 and 2021/2022 seasons separately.	1
EC$_a$	–	1
Elevation	–	1
Slope	–	1
Total daily rainfall	The rainfall amounts on each day of the 30-day period beforehand was used as a predictor.	30
Total daily PET	The PET amounts on each day of the 30-day period beforehand was used as a predictor.	30
Irrigation and Fertigation	The water input amounts, either sourced from irrigation or fertigation, on each day of the 30-day period beforehand was used as a predictor.	30
Plucking and Trimming	The occurrence of the events on each day of the 30-day period beforehand was used as a predictor.	30
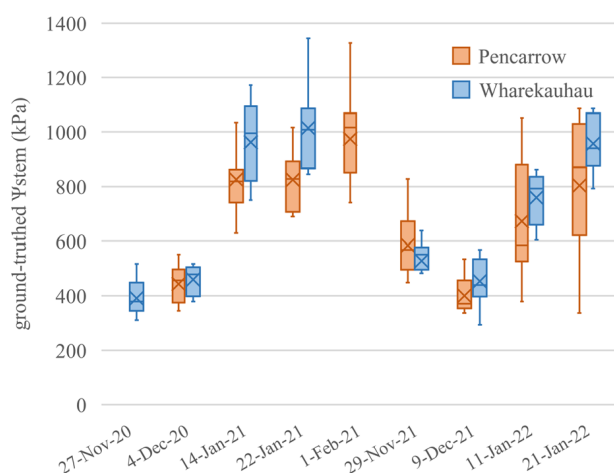
Fig. 5 Box plot of measured Ψstem collected during two growing seasons at Pencarrow (n = 86) and Wharekauhau (n = 62) vineyards. X symbols refer to the average values on the survey dates. Horizontal lines in the boxes refer to median values on the survey dates.

Ψstem obtained at Pencarrow were lower than those obtained at Wharekauhau on most of the measurement dates.

Modeling Performance

The regression modeling was conducted for the two-stage calibration (Fig. 3a & e) and the development of the Ψstem prediction model (Fig. 3g) using RFR, SVR, and MLP. The ML models with the best performance (in terms of RMSE on the test sets) were chosen (Table 4). The RMSE of the test sets for two-stage calibration, ranging from 59 to 113 kPa, indicates that the estimation obtained from the calibration models is well correlated with measured Ψstem (first calibration) and reference Ψstem (second calibration; Fig. 3c). Therefore, the calibrated satellite images (Fig. 3f) should serve as a robust reference as response variables for Ψstem prediction (Fig. 3g).

The RMSE of the test sets for Ψstem prediction is 31 kPa, suggesting the prediction model adequately captured Ψstem variability in 2020/2021. The scatter plots (Fig. 6) show that the data distribution for each regression model is closely clustered around the 1:1 line.

The Accuracy of the Spatial and Temporal Patterns of Ψstem Prediction

An important goal of this study was to validate whether a Ψstem prediction model based only on the first-season data (2020/2021) can be used to predict Ψstem changes in the second season (2021/2022). The similarity analysis, between Ψstem prediction maps (obtained from the best prediction model) and the Ψstem reference maps (obtained from 3m calibrated UAV images in 2021/2022) was conducted using Pearson correlation for each vineyard. The values of r represent the degree of consistency between predicted and reference maps across multiple survey dates, with p-values showing a significant association (Table 5).

Figure 7 shows Ψstem prediction alongside measured Ψstem values (collected by grid sampling throughout the study periods in 2021/2022) during the season for both vineyards. Ψstem predictions were normalized for better visualization. Both Ψstem prediction series for both vineyards appear to intercept with each of the spreads of measured Ψstem data approximately at their average value, except for the last measurements at Wharekauhau vineyard. Note that higher Ψstem values indicate more dehydrated vines. Measured Ψstem values are assumed to represent the total variability of each vineyard. Thus, this result indicates that the temporal patterns in 2020/2021 captured by the Ψstem prediction model can provide good temporal predictions during the study period in 2021/2022.

Descriptive statistics, including mean, standard deviation (SD), and coefficient of variation (CV), are presented in Table 6 to help assess the 2021/2022 datasets of measured Ψstem

Table 4. Results of modeling performance. UAV is uncrewed aerial vehicle; Ψstem is stem water potential; RMSE is root mean square error.

Modeling Purpose	Regression Model	Data Size of Measured or Reference Ψstem	RMSE of the Training Set (kPa)	RMSE of the Test Set (kPa)
Calibration of UAV images acquired in 2020/2021 (Fig. 3a)	Multilayer perceptron	85	96	113
Calibration of UAV images acquired in 2021/2022 (Fig. 3a)	Random forest regression	63	121	106
Calibration of Satellite images (Fig. 3e)	Random forest regression	42,234	47	59
Prediction of Ψstem (Fig. 3g)	Random forest regression	151,580	25	31
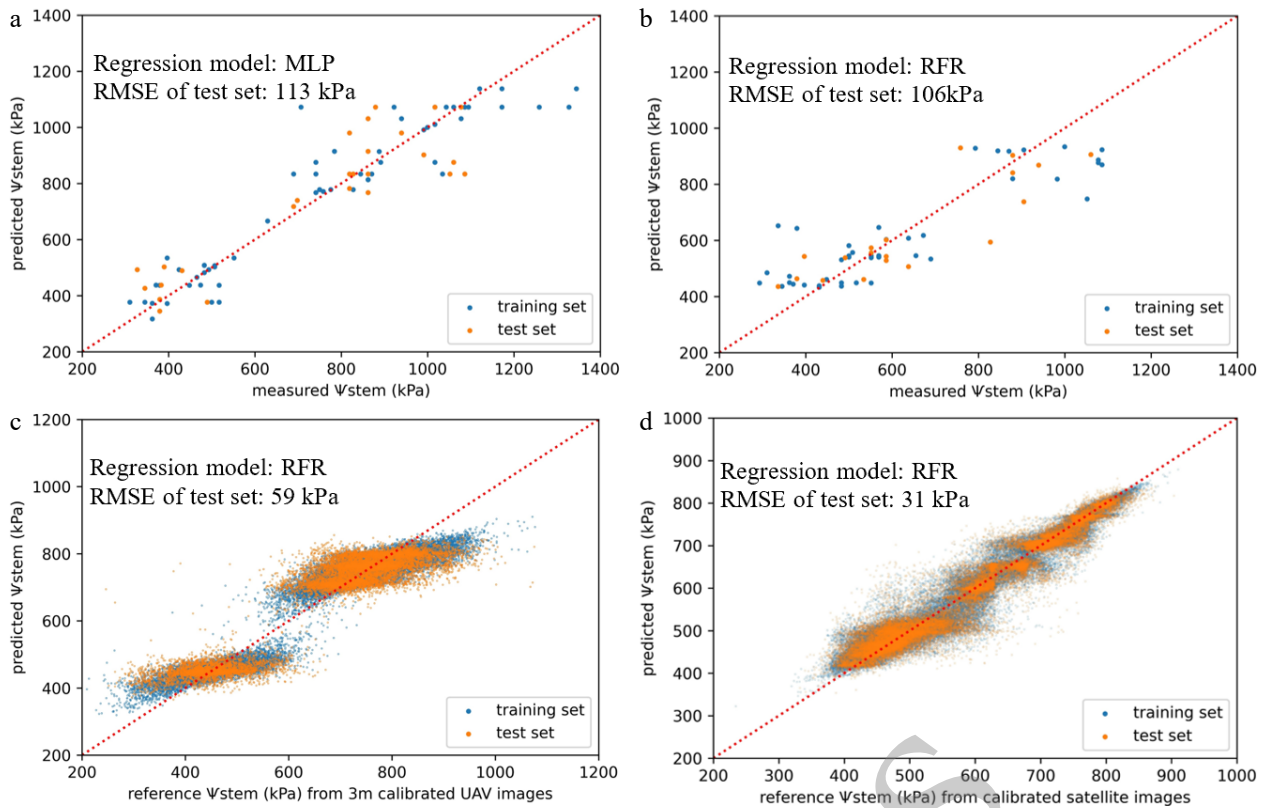
Fig. 6 Scatter plots between predicted Ψstem and measured or reference Ψstem (kPa) for the training and test sets of 6a: the calibration of UAV images acquired in 2020/2021. 6b: the calibration of UAV images acquired in 2021/2022. 6c: the calibration of satellite (PS) images. 6d: the prediction of Ψstem in 2020/2021. Red dashed lines are 1:1 lines. Samples from the two study vineyards are considered collectively in each regression model.

Table 5. Results of similarity analysis, presented by the Pearson correlation coefficient (r), represent the consistency between predicted and reference Ψstem maps across four survey dates for the two study vineyards.

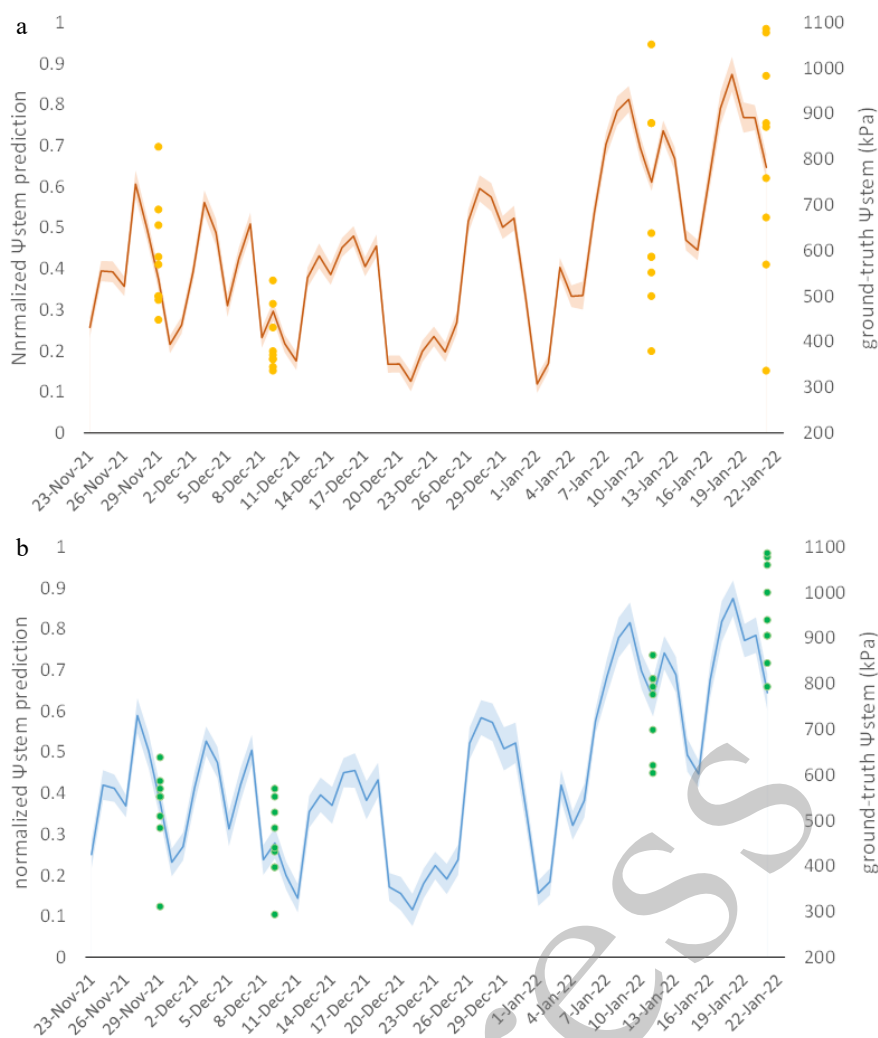|	Pencarrow	Wharekauhau
r	0.89*	0.87*

Significance levels are noted as * when p ≤ 0.001

values, reference Ψstem values obtained from 3 m calibrated UAV images, and predicted Ψstem values generated by the Ψstem prediction model. The statistics indicate that measured Ψstem values (CV > 10%) were more heterogeneous than the Ψstem values in the corresponding 3m calibrated UAV datasets (4% > CV > 2%) and the prediction datasets (CV < 2%). Thus, the tendency to exhibit extreme Ψstem values decreases from the 3 m calibrated UAV datasets (n = 42234, Ψstem $_{max}$ = 867, Ψstem $_{min}$ = 473) to the prediction datasets (n = 151,580, Ψstem $_{max}$ = 694, Ψstem $_{min}$ = 550) compared to the measured datasets (n = 63, Ψstem $_{max}$ = 1,086 kPa, Ψstem $_{min}$ = 293 kPa). Although there are differences in the absolute values and variability of Ψstem for the three datasets, they approximately follow the same temporal patterns over the study period in 2021/2022 (Fig. 8). This indicates that both 3m calibrated UAV datasets and Ψstem prediction datasets are more reliable predictors of the temporal patterns of Ψstem, rather than their absolute values.

Discussion

Reference Ψstem Data Generated by Two-Stage Calibration

To generate reference Ψstem data for subsequent prediction modeling, two-stage calibration was employed to calculate Ψstem data from satellite images based on measured Ψstem data using RFR, SVR, and MLP. Satellite images (obtained from PS in this study) have advantages over UAV data or measured data, in terms of higher coverage during one acquisition and regular acquisition periods. Therefore, satellite images are a better source in terms of providing observations on a regular basis. However, when assessing vertically-oriented grapevine status with discontinuous layouts, the utilization of low-to-moderate satellite resolution is often challenging due to the biased estimation resulting from pixels with mixed signals[10]. To address the issue of mixed-signal pixels, two calibration events were applied to scale the measured measurements up to data at the 3 m satellite level. UAV-based data served a critical role in this approach as it enhanced spectral purity by removing non-grapevine pixels and provided a large number of 0.05m reference data, which was then spatially aggregated to ensure scale matching between satellite data and measurements[13,14]. The performance (in terms of RMSE on the test sets) of the first and the second calibration for the data acquired in 2020/2021 was 113 and 59 kPa, respectively (Table 4). These results supported the appropriateness of this two-stage calibration approach in generating large reference datasets (n = 151,580), compared to the measured samples (n =

Fig. 7 The temporal patterns of normalized Ψstem prediction (lines) during the growing season in 2021/2022, with the measured Ψstem measurements (points) for Pencarrow (7a) and Wharekauhau (7b). The shaded bands bordering the lines encompass one standard deviation.

Table 6. Summary statistics for predicted Ψstem, Ψstem acquired from 3m calibrated UAV images, and measured Ψstem for each survey date at the Pencarrow and Wharekauhau vineyards. UAV is uncrewed aerial vehicle; SD is standard deviation; CV is coefficient of variation.

Survey Date	Vineyard	Data Source	Mean	SD	CV
29th November 2021	Pencarrow	Predicted Ψstem	609	5.59	0.92
		Ψstem from 3m calibrated UAV	562	18.11	3.22
		Measured Ψstem	585	113.93	19.47
	Wharekauhau	Predicted Ψstem	603	9.26	1.53
		Ψstem from 3m calibrated UAV	565	21.86	3.87
		Measured Ψstem	528	87.31	16.55
09th December 2021	Pencarrow	Predicted Ψstem	593	5.03	0.85
		Ψstem from 3m calibrated UAV	547	15.19	2.78
		Measured Ψstem	400	64.25	16.05
	Wharekauhau	Predicted Ψstem	580	8.95	1.54
		Ψstem from 3m calibrated UAV	548	17.42	3.18
		Measured Ψstem	453	82.18	18.14
11th January 2022	Pencarrow	Predicted Ψstem	662	4.84	0.73
		Ψstem from 3m calibrated UAV	681	19.53	2.87
		Measured Ψstem	672	204.27	30.39
21st January 2021	Pencarrow	Predicted Ψstem	670	6.73	1.01
		Ψstem from 3m calibrated UAV	717	22.86	3.19
		Measured Ψstem	803	233.27	29.03
	Wharekauhau	Predicted Ψstem	668	10.35	1.55
		Ψstem from 3m calibrated UAV	740	24.67	3.34
		Measured Ψstem	957	99.35	10.39
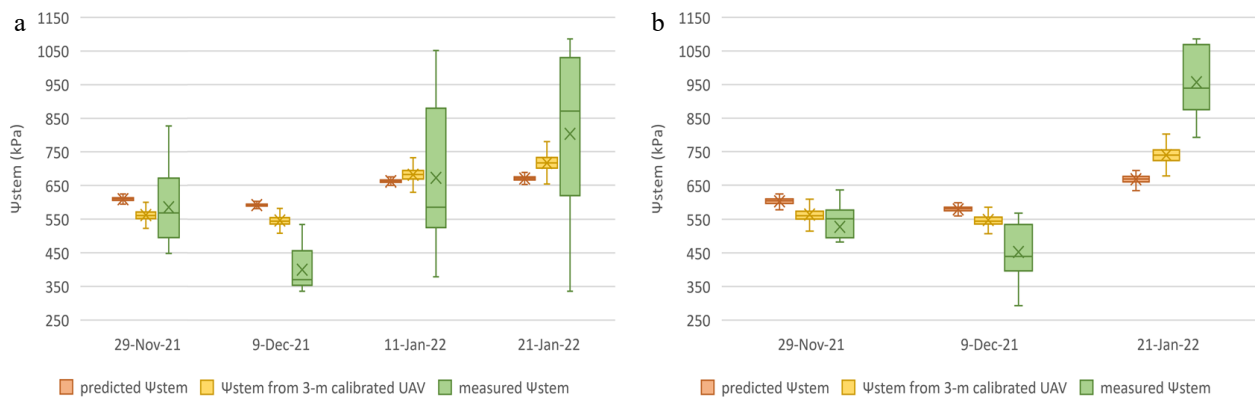
Fig. 8 Box plots of predicted Ψstem values, Ψstem values acquired from 3m calibrated UAV images, and measured Ψstem values for each survey date at the Pencarrow (8a) and Wharekauhau (8b) vineyards. UAV is uncrewed aerial vehicle, and Ψstem is stem water potential.

85), for later modeling purposes.

Predicted Ψstem Data Generated by Ψstem Prediction Model

The Ψstem prediction model was developed using calibrated PS images acquired in 2020/2021 as response variables, and using NDVI, EC_a, elevation, slope, DOY, irrigation, fertigation, plucking, and trimming events, daily total rainfall, and daily total PET as predictors. The need for this Ψstem prediction model was demonstrated by the number of PS acquisition images in this study. As the revisit period of PS is daily, there should potentially be 80 images, with surface reflectance assets, proper ground control, and standard quality, available over the study periods during 2020/2021 (15th November 2020 to 2nd February 2021). Nevertheless, there were only 20 images available to download, with only 13 images (the longest time gap between acquisition dates being 17 days) suitable for analysis (after eliminating those images contaminated with cloud, haze, or cloud shadow). Bellvert et al.[63] have suggested access to five to six points of information acquisition over the season for vineyard irrigation scheduling when considering cost efficiency. To avoid inaccessible satellite data caused by weather or technical problems, the development of a GWS prediction model is desirable.

The trained model performed well on the test set of data obtained in 2020/2021, with an RMSE of 31 kPa on the test sets (Table 4). From the two-stage calibration to Ψstem prediction, it appears the accuracy of modeling was higher as the data size of measured or reference Ψstem increased, resulting from the two-stage calibration. This confirmed that ML models develop more robust relationships with fewer overfitting issues when they are trained with more samples[64]. The superior performance of RFR with calibration and prediction modeling is probably because RFR is robust to multicollinearity[65]. Multicollinearity was evident in the datasets of this study, originating from VI computation based on the same spectral band, and temporal autocorrelation between the rainfall and PET data series.

In this study, the model was further evaluated with the data independently collected during a second growing season (2021/2022) to test its generalization performance. The model reflected the trends of changes of Ψstem in response to measured Ψstem. The predicted temporal patterns became more hydrated in early December compared to late November but exhibited increasing water deficit as the growing season

proceeded, which is comparable to measured Ψstem data (Figs 5 and 7). Similarity analysis (in terms of r) indicated that temporal patterns were well depicted by the prediction models for both vineyards (Table 5). It should be noted that the model's prediction capability was evaluated using calibrated UAV images (reference maps) instead of using measured Ψstem. The reason for this is the output of the prediction model is 3-m spatial resolution, and each pixel corresponds to multiple grapevines. Thus, the outputs cannot be directly compared with individually measured Ψstem. Besides, PS images acquired in 2021/2022 cannot be used for evaluation because background information (soil and grass) is included. Therefore, the prediction model was evaluated using the calibrated UAV images that approximated the measured Ψstem assumed to represent the total GWS variability across the study vineyards (RMSE = 106 kPa). The results of similarity analysis may be attributed to the observed similarity in PET variability over the two seasons (Fig. 2). As ET is a critical component in the soil water balance contributing to Ψstem[66], the similarity of ET from different seasons may lead to a similarity in the temporal variation of Ψstem over different years. Another reason for the similarity is that cultivation practices were applied within similar timeframes during each growing season, so their impacts were still within the prediction range of the model. In addition, both NDVI-defined and EC_a-defined zones have been reported to support spatial assessment of GWS[58,67], further increasing the prediction capabilities of the model.

The prediction model established the temporal variation of Ψstem based on DOY, 30-day total daily rainfall, 30-day total daily PET, 30-day irrigation, 30-day fertigation, 30-day plucking, and 30-day trimming, while accounting for the spatial variation of Ψstem based on NDVI, EC_a, elevation, and slope. Although temporal patterns of Ψstem were tested with promising results, it should be noted that the relative pattern of values, rather than their absolute values, should be the focus of attention in this study. Therefore, sampling for Ψstem prediction should be undertaken at the beginning of each growing season for model calibration, so as to enhance the precision and practicability of the model for use in irrigation scheduling.

Limitations and Directions for Future Research

The weakness of the prediction model in this study lies in its empirical approach, so it is unable to provide a reliable prediction if the inputs are beyond the range of observed variability. Field measurements are needed to validate the

prediction model with data collected from additional phenological stages, growing seasons, and sites, to enhance the model's scope. In addition, due to the selection of 3m resolution satellite images, high heterogeneity of GWS within a cell of grids would be averaged and exhibit less variation in Ψstem, thus introducing bias into calibration and modeling.

In its current form, this prediction model will only be able to predict Ψstem at vineyard-block scale during the growing season, rather than provide a spatial map of Ψstem each day. One reason is that weather predictors (including daily total rainfall, and daily total PET) were assumed to be evenly spatially distributed across the two vineyards. Predictors accounting for spatial variation (including NDVI, ECa, elevation, and slope) are static during modeling and are determined before the growing seasons. Despite these limitations, this prediction model is still a potentially practical tool for viticulturists since the block size of the results can be adjusted, by increasing the number of weather sensors or stations, to suit the size of zones that need different irrigation management.

Subsequent research is suggested to explore new predictor variables that are cost-effective to acquire and can serve as spatio-temporal proxies for Ψstem. Weather parameters, recorded spatially and continuously by wireless sensor networks across vineyards, could be one of these potential predictors. Further research work should examine the number and type of field measurements required and protocols needed for vineyard sampling to contribute to model calibration at the beginning of the growing season. The impact of the quality of weather forecasts on the performance of the prediction model also requires investigation. This will, potentially, allow the model to become a more reliable prediction tool, providing daily Ψstem spatial maps in advance throughout the growing season.

Conclusions

This study demonstrated the potential application of using a two-stage calibration approach for calibrating satellite images to provide reference stem water potential (Ψstem) data. The potential of establishing a Ψstem prediction model based on day of the year, normalized difference vegetation indices, apparent electrical conductivity, elevation, slope, rainfall, potential evapotranspiration, irrigation, fertigation, plucking, and trimming events, was also demonstrated. Collection of ground truthing is required for model calibration at the beginning of the growing season. The prediction model can be improved on a daily basis if predictors that account for spatio-temporal variability in Ψstem are provided, such as spatially recorded weather information. This tool has the potential to benefit vineyard managers with improved irrigation management and quality optimization by providing Ψstem predictions at vineyard-block scale during growing seasons, when the model is properly calibrated and coupled with accurate weather forecasts.

Acknowledgments

Conflict of interest

The authors declare that they have no conflict of interest.

Dates

References

1. Ojeda H, Andary C, Kraeva E, Carbonneau A, Deloire A. 2002. Influence of pre-and postveraison water deficit on synthesis and concentration of skin phenolic compounds during berry growth of Vitis vinifera cv. Shiraz. *American Journal of Enology and Viticulture* 53:261−7

2. Van Leeuwen C, Trégoat O, Choné X, Bois B, Pernet D, Gaudillère J-P. 2009. Vine water status is a key factor in grape ripening and vintage quality for red Bordeaux wine. *How can it be assessed for vineyard management purposes? OENO One* 43:121−34

3. Martínez-Lüscher J, Sánchez-Díaz M, Delrot S, Aguirreolea J, Pascual I, et al. 2014. Ultraviolet-B radiation and water deficit interact to alter flavonol and anthocyanin profiles in grapevine berries through transcriptomic regulation. *Plant and Cell Physiology* 55:1925−36

4. Chaves M, Zarrouk O, Francisco R, Costa J, Santos T, et al. 2010. Grapevine under deficit irrigation: hints from physiological and molecular data. *Annals of botany* 105:661−76

5. Brillante L, Martinez-Luscher J, Yu R, Plank CM, Sanchez L, et al. 2017. Assessing spatial variability of grape skin flavonoids at the vineyard scale based on plant water status mapping. *Journal of agricultural and food chemistry* 65:5255−65

6. Bramley R, Ouzman J, Boss PK. 2011. Variation in vine vigour, grape yield and vineyard soils and topography as indicators of variation in the chemical composition of grapes, wine and wine sensory attributes. *Australian Journal of Grape and Wine Research* 17:217−29

7. Arnó Satorra J, Martínez Casasnovas JA, Ribes Dasi M, Rosell Polo JR. 2009. Precision viticulture. Research topics, challenges and opportunities in site-specific vineyard management. *Spanish Journal of Agricultural Research, 2009, vol. 7, núm. 4, p. 779−790*

8. Monaghan JM, Daccache A, Vickers LH, Hess TM, Weatherhead EK, et al. 2013. More 'crop per drop': constraints and opportunities for precision irrigation in European agriculture. *Journal of the Science of Food and Agriculture* 93:977−80

9. Matese A, Toscano P, Di Gennaro S, Genesio L, Vaccari F, et al. 2015. Intercomparison of UAV, Aircraft and Satellite Remote Sensing Platforms for Precision Viticulture. *Remote Sensing* 7:2971−90

10. Borgogno-Mondino E, Lessio A, Tarricone L, Novello V, De Palma L. 2018. A comparison between multispectral aerial and satellite imagery in precision viticulture. *Precision Agriculture* 19:195−217

11. Khaliq A, Comba L, Biglia A, Ricauda Aimonino D, Chiaberge M, Gay P. 2019. Comparison of satellite and UAV-based multispectral imagery for vineyard variability assessment. *Remote Sensing* 11:436

12. Helman D, Bahat I, Netzer Y, Ben-Gal A, Alchanatis V, et al. 2018. Using time series of high-resolution planet satellite images to monitor grapevine stem water potential in commercial vineyards. *Remote Sensing* 10:1615

13. Pla M, Bota G, Duane A, Balagué J, Curcó A, et al. 2019. Calibrating Sentinel-2 imagery with multispectral UAV derived information to quantify damages in Mediterranean rice crops caused by Western Swamphen (Porphyrio porphyrio). *Drones* 3:45

14. Revill A, Florence A, MacArthur A, Hoad S, Rees R, Williams M. 2020. Quantifying uncertainty and bridging the scaling gap in the retrieval of leaf area index by coupling Sentinel-2 and UAV observations. *Remote Sensing* 12:1843

15. Bukowiecki J, Rose T, Kage H. 2021. Sentinel-2 Data for Precision Agriculture?—A UAV-Based Assessment *Sensors* 21:2861

16. Mazzia V, Comba L, Khaliq A, Chiaberge M, Gay P. 2020. UAV and machine learning based refinement of a satellite-driven vegetation index for precision agriculture. *Sensors* 20:2530

17. Gautam D, Pagay V. 2020. A review of current and potential applications of remote sensing to study the water status of horticultural crops. *Agronomy* 10:140

18. Brook A, De Micco V, Battipaglia G, Erbaggio A, Ludeno G, et al. 2020. A smart multiple spatial and temporal resolution system to support precision agriculture from satellite images: Proof of concept on Aglianico vineyard. *Remote Sensing of Environment* 240:111679

19. Devaux N, Crestey T, Leroux C, Tisseyre B. 2019. Potential of Sentinel-2 satellite images to monitor vine fields grown at a territorial scale. *Oeno One* 53:52−9

20. van LEEUWEN C, GOUTOULY J-P, COSTA-FERREIRA A-M, AZAÏS C, MARGUERIT E, et al. 2006. Intra-block variations of vine water status in time and space Variations intra-parcellaires temporelles et spatiales du régime hydrique de la vigne. *Vine*: 64−9

21. Jasse A, Berry A, Aleixandre-Tudo JL, Poblete-Echeverría C. 2021. Intra-block spatial and temporal variability of plant water status and its effect on grape and wine parameters. *Agricultural Water Management* 246:106696

22. Allen RG, Pereira LS, Raes D, Smith M. 1998. Crop evapotranspiration-Guidelines for computing crop water requirements-FAO Irrigation and drainage paper 56. *Fao, Rome* 300:D05109

23. Bellvert J, Marsal J, Mata M, Girona J. 2012. Identifying irrigation zones across a 7.5-ha 'Pinot noir'vineyard based on the variability of vine water status and multispectral images. *Irrigation Science* 30:499−509

24. Ohana-Levi N, Munitz S, Ben-Gal A, Netzer Y. 2020. Evaluation of within-season grapevine evapotranspiration patterns and drivers using generalized additive models. *Agricultural Water Management* 228:105808

25. Suter B, Triolo R, Pernet D, Dai Z, Van Leeuwen C. 2019. Modelling stem water potential by separating the effects of soil water availability and climatic conditions on water status in grapevine (Vitis vinifera L.). *Frontiers in Plant Science* 10:1485

26. Kuhn M, Johnson K. 2013. *Applied predictive modeling*. Springer

27. Borgogno-Mondino E, Novello V, Lessio A, de Palma L. 2018. Describing the spatio-temporal variability of vines and soil by satellite-based spectral indices: A case study in Apulia (South Italy). *International journal of applied earth observation and geoinformation* 68:42−50

28. Matese A, Baraldi R, Berton A, Cesaraccio C, Di Gennaro SF, et al. 2018. Estimation of water stress in grapevines using proximal and remote sensing methods. *Remote Sensing* 10:114

29. Baluja J, Diago MP, Balda P, Zorer R, Meggio F, et al. 2012. Assessment of vineyard water status variability by thermal and multispectral imagery using an unmanned aerial vehicle (UAV). *Irrigation Science* 30:511−22

30. Espinoza CZ, Khot LR, Sankaran S, Jacoby PW. 2017. High resolution multispectral and thermal remote sensing-based water stress assessment in subsurface irrigated grapevines. *Remote Sensing* 9:961

31. Poblete T, Ortega-Farias S, Moreno MA, Bardeen M. 2017. Artificial Neural Network to Predict Vine Water Status Spatial Variability Using Multispectral Information Obtained from an Unmanned Aerial Vehicle (UAV). *Sensors (Basel)* 17

32. Romero M, Luo Y, Su B, Fuentes S. 2018. Vineyard water status estimation using multispectral imagery from an UAV platform and machine learning algorithms for irrigation scheduling management. *Computers and Electronics in Agriculture* 147:109−17

33. Wei H-E, Grafton M, Bretherton M, Irwin M, Sandoval E. 2021. Evaluation of point hyperspectral reflectance and multivariate regression models for grapevine water status estimation. *Remote Sensing* 13:3198

34. Wei H-E, Grafton M, Bretherton M, Irwin M, Sandoval E. 2022. Evaluation of the Use of UAV-Derived Vegetation Indices and Environmental Variables for Grapevine Water Status Monitoring Based on Machine Learning Algorithms and SHAP Analysis. *Remote Sensing* 14:5918

35. Fernandes-Silva A, Oliveira M, Paço TA, Ferreira I. 2019. Deficit irrigation in Mediterranean fruit trees and grapevines: Water stress indicators and crop responses. *Irrigation in Agroecosystems. London, United Kingdom*

36. Schreiner RP, Lee J. 2014. Effects of post-véraison water deficit on 'Pinot noir'yield and nutrient status in leaves, clusters, and musts. *HortScience* 49:1335−40

37. Patakas A, Noitsakis B, Chouzouri A. 2005. Optimization of irrigation water use in grapevines using the relationship between transpiration and plant water status. *Agriculture, Ecosystems & Environment* 106:253−9

38. Giovos R, Tassopoulos D, Kalivas D, Lougkos N, Priovolou A. 2021. Remote sensing vegetation indices in viticulture: A critical review. *Agriculture* 11:457

39. Gitelson AA, Viña A, Ciganda V, Rundquist DC, Arkebauer TJ. 2005. Remote estimation of canopy chlorophyll content in crops. *Geophysical Research Letters* 32

40. Tucker CJ. 1979. Red and photographic infrared linear combinations for monitoring vegetation. *Remote sensing of Environment* 8:127−50

41. Huete A, Didan K, Miura T, Rodriguez EP, Gao X, Ferreira LG. 2002. Overview of the radiometric and biophysical performance of the MODIS vegetation indices. *Remote sensing of environment* 83:195−213

42. Woebbecke DM, Meyer GE, Von Bargen K, Mortensen DA. 1995. Color indices for weed identification under various soil, residue, and lighting conditions. *Transactions of the ASAE* 38:259−69

43. Gitelson AA, Merzlyak MN. 1998. Remote sensing of chlorophyll concentration in higher plant leaves. *Advances in Space Research* 22:689−92

44. Daughtry CS, Walthall C, Kim M, De Colstoun EB, McMurtrey Iii J. 2000. Estimating corn leaf chlorophyll concentration from leaf and canopy reflectance. *Remote sensing of Environment* 74:229−39

45. Qi J, Chehbouni A, Huete AR, Kerr YH, Sorooshian S. 1994. A modified soil adjusted vegetation index. *Remote sensing of environment* 48:119−26

46. Haboudane D, Miller JR, Pattey E, Zarco-Tejada PJ, Strachan IB. 2004. Hyperspectral vegetation indices and novel algorithms for predicting green LAI of crop canopies: Modeling and validation in the context of precision agriculture. *Remote sensing of environment* 90:337−52

47. Barnes E, Clarke T, Richards S, Colaizzi P, Haberland J, et al. Coincident detection of crop water stress, nitrogen status and canopy density using ground based multispectral data. *Proc. Proceedings of the Fifth International Conference on Precision Agriculture, Bloomington, MN, USA, 2000*, 1619:

48. Rouse J, Haas R, Schell J, Deering D, Harlan J. 1974. Monitoring the vernal advancements and retrogradation. *Texas AM Univ, Texas*

49. Rondeaux G, Steven M, Baret F. 1996. Optimization of soil-adjusted vegetation indices. *Remote sensing of environment* 55:95−107

50. Gamon J, Surfus J. 1999. Assessing leaf pigment content and activity with a reflectometer. *The New Phytologist* 143:105−17

51. Birth GS, McVey GR. 1968. Measuring the color of growing turf with a reflectance spectrophotometer 1. *Agronomy Journal* 60:640−3

52. Haboudane D, Miller JR, Tremblay N, Zarco-Tejada PJ, Dextraze L. 2002. Integrated narrow-band vegetation indices for prediction of crop chlorophyll content for application to precision agriculture. *Remote sensing of environment* 81:416−26

53. Gitelson AA, Kaufman YJ, Stark R, Rundquist D. 2002. Novel algorithms for remote estimation of vegetation fraction. *Remote sensing of Environment* 80:76−87

54. Planet Team. 2017. Planet application program interface: In space for life on earth. *San Francisco*

55. Leach N, Coops NC, Obrknezev N. 2019. Normalization method for multi-sensor high spatial and temporal resolution satellite imagery with radiometric inconsistencies. *Computers and Electronics in Agriculture* 164:104893

56. Houborg R, McCabe MF. 2018. Daily Retrieval of NDVI and LAI at 3 m Resolution via the Fusion of CubeSat, Landsat, and MODIS Data. *Remote Sensing* 10:890

57. Cook PG, Williams BG. 1998. *Electromagnetic Induction Techniques-Part 8*. CSIRO PUBLISHING

58. Yu R, Brillante L, Martínez-Lüscher J, Kurtural SK. 2020. Spatial Variability of Soil and Plant Water Status and Their Cascading Effects on Grapevine Physiology Are Linked to Berry and Wine Chemistry. *Frontiers in Plant Science* 11

59. Penman HL. Natural evaporation from open water, bare soil and grass. *Proc. Proceedings of the Royal Society of London, 1948*, 193: 120-45:

60. Willwerth JJ, Reynolds AG. 2020. Spatial variability in Ontario Riesling Vineyards: I. Soil, vine water status and vine performance. *Oeno One* 54:311−33

61. Kazmierski M, Glémas P, Rousseau J, Tisseyre B. 2011. Temporal stability of within-field patterns of NDVI in non irrigated Mediterranean vineyards. *Oeno One* 45:61−73

62. Heil K, Schmidhalter U. 2017. The application of EM38: Determination of soil parameters, selection of soil sampling points and use in agriculture and archaeology. *Sensors* 17:2540

63. Bellvert J, Zarco-Tejada PJ, Marsal J, Girona J, González-Dugo V, Fereres E. 2016. Vineyard irrigation scheduling based on airborne thermal imagery and water potential thresholds. *Australian Journal of Grape and Wine Research* 22:307−15

64. Lever J, Krzywinski M, Altman N. 2016. Points of significance: model selection and overfitting. *Nature methods* 13:703−5

65. Zhan Y, Luo Y, Deng X, Zhang K, Zhang M, et al. 2018. Satellite-based estimates of daily NO2 exposure in China using hybrid random forest and spatiotemporal kriging model. *Environmental science & technology* 52:4180−89

66. Montoro A, López Urrea R, Mañas F, López Fuster P, Fereres E. 2006. Evapotranspiration of grapevines measured by a weighing lysimeter in La Mancha, Spain. *Proc. V International Symposium on Irrigation of Horticultural Crops* 792:459−66

67. Acevedo-Opazo C, Tisseyre B, Guillaume S, Ojeda H. 2008. The potential of high spatial resolution information to define within-vineyard zones related to vine water status. *Precision Agriculture* 9:285−302